Ocean Engineering 285 (2023) 115335

Contents lists available at ScienceDirect

Ocean Engineering

journal homepage: www.elsevier.com/locate/oceaneng

Underwater collision avoidance using undulating elongated fin propulsion

Mohammad Uddin [*], Gonzalo Garcia, Oscar Curet [**]

Florida Atlantic University, Department of Ocean and Mechanical Engineering, 777 Glades Road, Boca Raton, FL, 33431, USA

ARTICLE INFO

Handling Editor: Prof. A.I. Incecik

Keywords:
Bio-propulsion
AUV
Biomimetics
Underwater robotics
Elongated fin propulsion
Collision avoidance

ABSTRACT

Underwater navigation to survey littoral regions or complex environments such as offshore structures, coral reefs or sensitive coastal zones requires a highly maneuverable propulsion mechanism. Conventional propulsors have limited maneuverability, often incapable of providing adequate torques and forces to maneuver in such environments. Elongated ribbon fin propulsion, a bio-inspired propulsion technique, can overcome these shortcomings. In the present work, we used a robotic vessel with elongated fin propulsion to test and implement three collision avoidance strategies based on potential field methods. We found that having a circular sensing envelope in the robotic vessel helps to smoothly transition to the mission path after collision is avoided. However, under this strategy, the distance to return to the desired path tends to be longer. The selection of adequate collision avoidance strategies will depend on multiple factors, including others sensing capabilities, desired reaction time, rate of turning and objects to avoid. Although this work focused on relatively simple scenarios for obstacle avoidance, we envision that utilizing more complex maneuver techniques, including rapid turns and hovering, collision avoidance strategies for underwater vessels with undulating fin propulsion can take advantage of the full fin kinematics manipulation to maneuvers as elegant as seen on the fish counterpart.

1. Introduction

Bio-inspired underwater propulsions can enhance maneuverability at low speed with negligible acoustic signature and thus allow underwater survey and navigation in complex underwater environments such as littoral zones, reef monitoring, offshore structure inspection, among other scenarios. Collision avoidance has long trajectory for underwater vehicles using conventional propulsion systems (Braginsky and Guterman, 2016; Lapierre and Jouvencel, 2008). However, there has been very limited work on how collision avoidance techniques can be implemented to bio-inspired propulsion. In this work, we focused on a vessel with an elongated ribbon fin propulsion and a limited sensory volume to avoid collision with an object while approaching a desired target point or path.

Elongated ribbon fin propulsion, inspired by the anal fin of black ghost knifefish shown in Fig. 1a, is of particular interest because it can provide a wide control of propulsive forces even at low speed, where conventional propulsors do not perform well. Using a robotic elongated fin, previous research showed that this propulsion mechanism can perform different maneuvers including forward (Liu and Curet, 2018), reverse, upward swimming, as well as turning and keep station (Curet et al., 2011a). Given the maneuverability of this type of propulsion, it is essential to implement a collision avoidance scheme that works in conjunction with an undulating fin propulsion. Even though the capability of the elongated ribbon fin propulsion technique has been demonstrated, there has been no prior experimental work on collision avoidance by a robotic elongated fin propulsion. In this work, we present experimental results for different collision avoidance strategies, conducted by a robotic vessel (Fig. 1b) with undulating elongated fin propulsion.

In elongated fin propulsion, waves are propagated along the fin (e.g. from one end to the other), generating thrust and motion in the opposite direction. The knifefish usually exhibits abrupt change in the direction of the traveling wave to reverse its swimming direction. Moreover, it is observed that fishes use two counter propagative waves, colliding at the center of the fin to hover or even provide an upward thrust (Curet et al., 2011a). Although the potential of robotic undulating fin propulsion is well investigated and documented in earlier works (Curet et al., 2011a, 2011b; Uddin and Curet, 2018; Liu and Curet, 2018; Uddin et al., 2020, 2022; Garcia et al., 2020), the present work aims to evaluate different collision strategies in conjunction with undulating fin propulsion. Recent work by Uddin et al. (2022) experimentally showed that the

---

[*] Corresponding author.

[**] Corresponding author.

E-mail addresses: muddin2017@fau.edu (M. Uddin), ocuret@fau.edu (O. Curet).

https://doi.org/10.1016/j.oceaneng.2023.115335
Received 28 November 2022; Received in revised form 5 July 2023; Accepted 6 July 2023
Available online 10 July 2023

force generated by undulating fin scales with square of the relative velocity between free streaming flow and wave speed in the robotic fin. In addition, they evaluated the efficiency of the propulsive fin for different kinematics and flow conditions. Hawkins et al. (2022) investigated turning maneuver of knifefish using 3D kinematics and descriptive DPIV.

Even though other bio-inspired propulsions, such as caudal fin like propulsion, have been investigated for collision avoidance (Sunkara et al., 2020), an autonomous underwater vessel with elongated fin propulsion has not been studied in detail yet. In this work, as a first step towards finding optimal collision avoidance strategy for undulating fin propulsion, we applied three different collision avoidance strategies (Sunkara et al., 2019, 2020) using an underwater vessel with undulating fin propulsion (Fan et al., 2020; Subramanian et al., 2012). In previous studies, collision avoidance by moving underwater vehicles has been studied for different cases (Subramanian et al., 2012; Subramanian et al., 2014; Chakravarthy and Ghose, 2018; I and Rivlin, 1998; Sosa and Adler; Li et al., 2019; Sunkara et al., 2019; Panda et al., 2020; Das et al., 2020; Han and Seo, 2017), across different propulsion mode and propulsion medium. Subramanian et al. (2012) presented an algorithm and simulation results for obstacle avoidance using a multi-point potential field approach. However, the collision avoidance method for any underwater propulsion mode must adapt to the need of that propulsion mechanism, as one method suitable to one propulsion mechanism can be unsuitable for the other.

In addition to the propulsion method, the sensory range and performance is an integral part of the collision avoidance strategy. In the case of the American knifefish (Gymnotiformes), they use a self-generated electric field in combination with electro receptors across its body to generate a short omni-directional sensory volume (Nelson and MacIver, 1999). This sensory volume in combination with its undulating ribbon fin allow the fish to detect small preys around its body and quickly react to capture them (Postlethwaite et al., 2009). In this work, we will consider two types of sensing areas: 1) sensing area with circular section profile and 2) a circular sensing area with a weighted factor. In addition, three different strategies using potential field methods to react to the obstacle are discussed and experimented with. While there is a common goal for all the strategies, i.e., avoiding

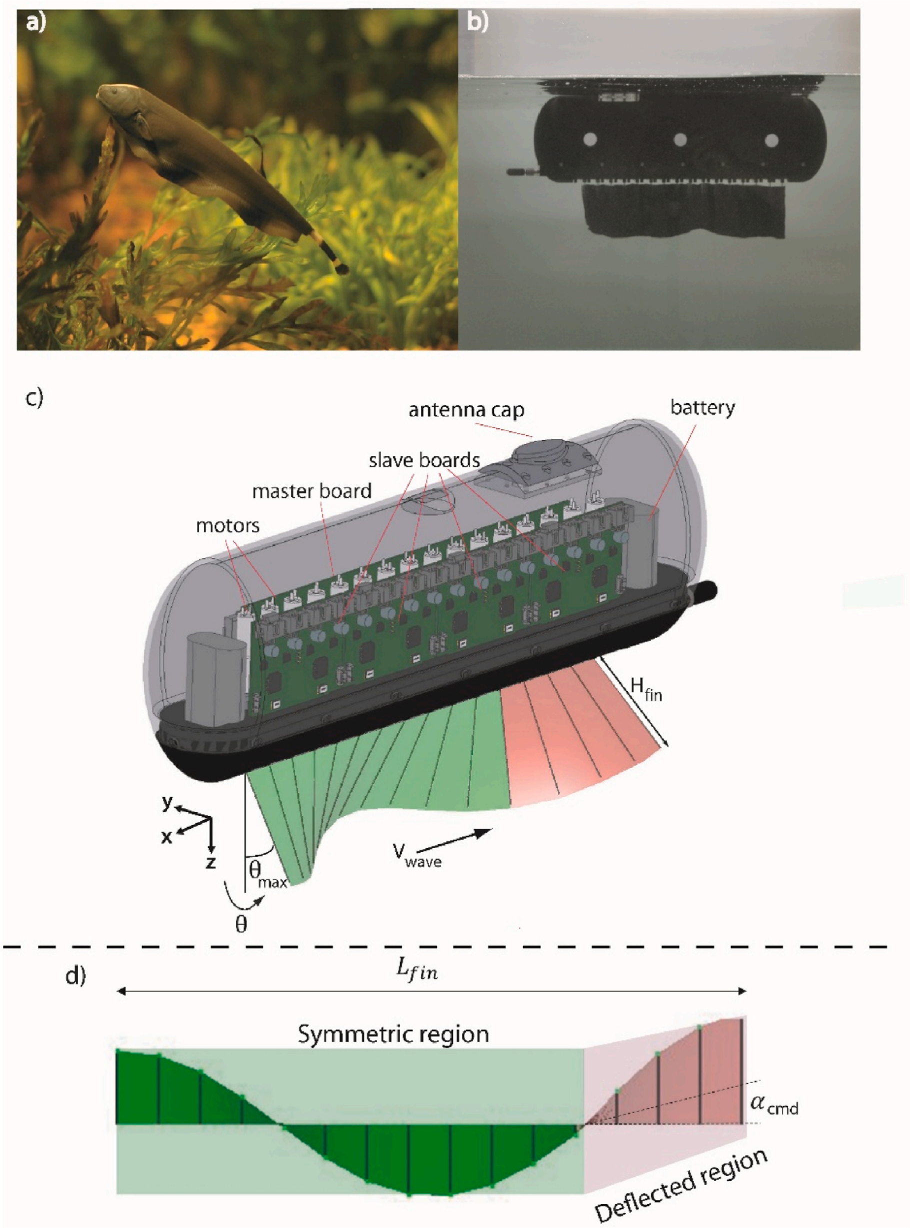

Fig. 1. The bio-inspired elongated ribbon fin propulsion. a) American black ghost knifefish swimming at its natural habitat (photo credit, Per Eric Sviland). B) Robotic fish (the Knifebot) swimming in laboratory water tank. c) 3D rendering of the robotic fish. The vessel features 16 motors, each actuating a flexible ray. d) Bottom view of the undulating fin. The rear portion (deflected region) of the fin is deflected to create an angle (α_{cmd}) to the centerline of the vessel, generating sway force and yaw moment for yaw maneuvering.

collision with a static obstacle, the missions vary for different strategies including reaching a target point considered for strategy 1 and, reaching target path considered for strategy 2 and 3 (see in Fig. 2). In all three cases, the obstacle is present in the trajectory of the vessel. Thus, the vessel reacts by changing the kinematics of the fin to avoid collision with the obstacle and once the path is clear, the vessel corrects its direction to approach the desired path or target point. The initial condition and obstacle size are varied for different strategies. To generate sway force and yaw moment for maneuvering, a simple thrust vectoring approach (Uddin and Curet, 2018, 2019; Garcia et al., 2022) is adopted where a portion of the fin generates thrust at an angle to the center line. As shown in Fig. 1c, the forward green portion of the fin undulates with its mean line aligned with the longitudinal axis, whereas the red portion close to the posterior undulates with mean axis oblique to the centerline of the vessel, hence providing sway force and yaw moment that helps maneuver the robotic vessel to avoid collision with obstacles encountered in the vessel's path. Although there are many other changes in kinematics that could be considered to provide changes in orientation, one of the motivations of this work is to present a simple but robust approach to control heading and obstacle avoidance with an undulating fin propulsion. In more complex maneuver scenarios such as rapid turns, hovering, we can envision the use of multiple counter-propagating waves as exhibited by the fish as well as determining optimal fin kinematics changes for specific maneuvers.

2. Material and methods

2.1. Bio-inspired robotic fish-the Knifebot

The bio-inspired robotic vessel shown in Fig. 1b was used for all the experiments presented in this work. The vessel is inspired by the propulsion mechanism used by the black ghost knifefish (*Apteronotus albifrons*). Snapshot of the vessel and 3D rendering of the robotic vessel are shown in Fig. 1b and c. The watertight hull of the vessel is comprised of an upper and the bottom hull. All the electronic components are mounted in the bottom hull.

Details on the components of the vessel are provided in (Uddin et al., 2022). The vessel has sixteen individual rays, each of which is actuated by an individual motor (RE10, Maxon Motor AG, Sachseln, Switzerland). The flexible membrane is composed out of Lycra fabric (30 cm × 7.7 cm). When the motors are actuated, the fin undergoes a sinusoidal motion with respect to the center line of the vessel, providing thrust necessary to propel the vessel. However, the last four rays of the vessel, shown in pink in Fig. 1c and d, are capable of oscillating with their axis oblique to the center line. This change in fin kinematics generates a non-zero average sway force as well as a rotating moment around the center of mass, enabling the vessel to perform 2D directional maneuvers.

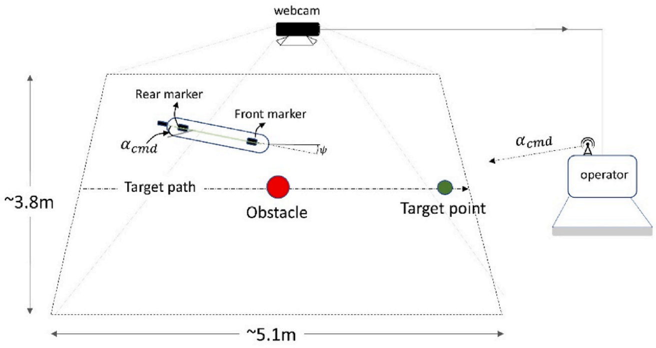

Fig. 2. Schematic diagram of experimental setup for collision avoidance experiment. The red circle indicates the obstacle. The goal of each experiment is either to reach the target (target point) or maintain position on a path (target path). The webcam takes snapshot at every sample time. Snapshot is post-processed at the operator station instantaneously to find the cartesian coordinates of the markers (front and rear).

To track the position and orientation of the robotic vessel, two rectangular black markers were constructed on top of it. The rest of the vessel was wrapped with white tape so that the markers have good contrast and can be tracked easily by processing the image captured from top of the vessel, as shown in Fig. 2. Although this approach is limited when operating on the surface, the main objective of the work was to demonstrate that when the position/orientation are known and the obstacle is detected, a real-time fin kinematics changes can be applied to avoid collision.

2.2. Collision avoidance strategies

In the present work, we will consider three different obstacle avoidance strategies based on the potential field approach. For all experiments, we have only considered one obstacle positioned along the vessel path to the target for strategy 1 and along the vessel mission path for strategy 2 and 3. Fig. 3 shows the close loop control algorithm used for collision avoidance experiments.

For each control loop, the key steps are described below.

1. First, the downward looking webcam, fastened at the top of the pool, captures a snapshot, which is processed by a MATLAB 2019 program that tracks the position of two markers on the top of the vessel. The position of the markers is then used to calculate the mean cartesian coordinate and yaw angle of the vessel at that time instant.
2. Given the diameter and position of the obstacle, a commanded yaw angle (ψ_{cmd}) is calculated. For the robotic vessel, ψ_{cmd} is the desired yaw angle with respect to the horizontal line (Fig. 2) while ψ is the actual yaw angle for a given time instant. The equation to calculate ψ_{cmd} depends on the collision strategy in use (Fig. 3). After that, the yaw error, (ψ_{err}), is calculated, which is defined as the difference between ψ and ψ_{cmd}. ψ_{err} is then used to calculate the desired deflection angle of fin, α_{cmd}. ψ_{err} and α_{cmd} are computed as follows.

$$\psi_{err}(t) = \psi_{cmd}(t) - \psi(t) \tag{1}$$

$$\alpha_{cmd}(t) = 0.833\psi_{err}(t) + 0.011\int \psi_{err}(t) \tag{2}$$

The integrator, $\int \psi_{err}(t)$, has an upper limit of 100. This is done to avoid typical integrator windup in a Proportional-Integral (PI) controller. The coefficients for Equation (2) were obtained first by simulating turning of the vessel based on torques and force models in the fin (Uddin and Curet, 2018; Uddin et al., 2022) and then fine-tuned by collision avoidance experiments with the robotic vessel.

3. The mean positions of rays 13–16, given by α_n, are calculated as follows.

$$\alpha_n(t) = (n - 12) \times \alpha_{cmd}(t) \tag{3}$$

Here, n = 13 − 16 (position of rays, from fore towards aft). Although the mean positions of these rays' change, the total undulation angle

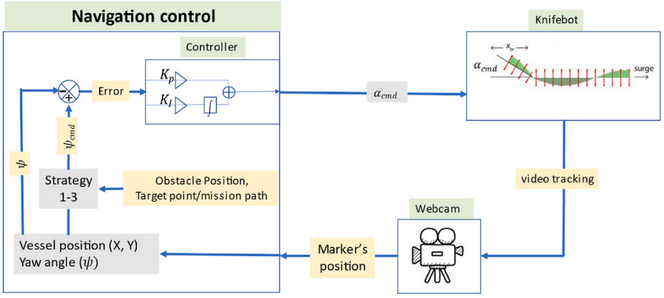

Fig. 3. Schematic diagram of close loop control for collision avoidance.

(swept angle) of these rays remains unchanged. However, the mean position of all other rays (position 1–12, from fore towards aft) does not change.

The webcam takes snapshots at regular time intervals. The mathematical formulations of these strategies are described below.

2.2.1. Strategy 1

The mission of this strategy required the robotic vessel to reach a point target, by avoiding collision with an upright cylindrical obstacle in its path. The schematic diagram explaining this strategy is given in Fig. 4. All the potential forces are considered acting on the center of gravity (*C.O.G.*) of the vessel. At all times, an attractive force, F_{att} acts towards the point target of the vessel, with unit magnitude ($F_{att} = 1$).

To sense the presence of the obstacle, we considered a virtual sensing envelope in front of the vessel. When the obstacle is partly or fully inside this sensing envelope, a repulsive force, F_{rep}, is generated, acting from the obstacle towards the vessel *C.O.G.* The magnitude of the repulsive force is given by.

$$F_{rep} = e^{-\left(\frac{D_{obs}}{L_{env}}\right)} \tag{4}$$

Here, D_{obs} is the distance between the obstacle's closest point to the vessel and *C.O.G.* of the vessel. The length of the collision cone is given by.

$$L_{env} = 3\,R_{obs} + L_{hull}$$

Where, R_{obs} is the radius of the obstacle and L_{hull} is the length of the vessel. The magnitude of F_{res} is the vector sum of F_{att} and F_{rep}.

$$\overrightarrow{F_{res}} = \overrightarrow{F_{att}} + \overrightarrow{F_{rep}} \tag{5}$$

Given that, the *C.O.G.* of the robotic vessel is at (x_v, y_v), and center of the obstacle is at (x_{obs}, y_{obs}), we define γ_{obs} as follows.

$$\gamma_{obs} = \tan^{-1}\left(\frac{y_{obs} - y_v}{x_{obs} - x_v}\right) \tag{6}$$

Now, γ_{res}, the angle between F_{res} and F_{att} is calculated as follows.

$$\gamma_{res} = \cos^{-1}\left(\frac{F_{res}^2 + F_{att}^2 - F_{rep}^2}{2F_{res}\,F_{att}}\right) \tag{7}$$

The commanded yaw angle, ψ_{cmd}, is the difference between γ_{res} and γ_{obs}.

$$\psi_{cmd} = \gamma_{res} - \gamma_{obs} \tag{8}$$

Considering an obstacle diameter of 0.54m ($R_{obs} = 0.27m$), and length of robotic vessel (L_{hull}) as 0.44m, L_{env} becomes 1.25m. On the other hand, an attractive force, F_{att}, acts from vessel *C.O.G.* towards the green target shown in Fig. 4, with unit magnitude ($F_{att} = 1$). The commanded yaw direction coincides with the direction of F_{res}, which is the resultant of F_{att} and F_{rep}. Therefore, when an obstacle is in the sensory envelop, the position of obstacle and the target simultaneously affect the commanded yaw angle by means of combination of repulsive and attractive force.

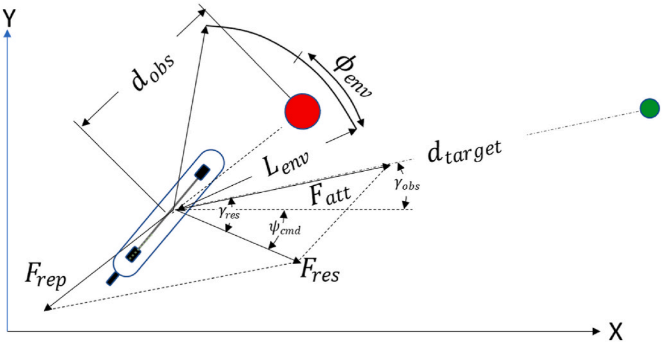

Fig. 4. Schematic diagram of collision avoidance under strategy 1. If the obstacle (or part of it) is inside the sensing envelope, the robot incurs F_{rep} that directs the vessel at a direction so that it could avoid collision with the obstacle.

2.2.2. Strategy 2

Strategy 2 requires the vessel to position itself on a target path. Like the previous strategy, the vessel considers a sensing envelope in search of any obstacle in its path. When obstacle is present inside the sensing envelope, both F_{att} and F_{rep} exist. The magnitude of F_{att} and F_{rep} are calculated as follows.

$$F_{att} = 1 \tag{9}$$

$$F_{rep} = e^{-\left(\frac{D_{obs}}{L_{env}}\right)} \tag{10}$$

Unlike strategy 1, F_{att} is always directed parallel to the target path (towards *x*-axis in Fig. 5). The magnitude of F_{res} is the vector sum of F_{att} and F_{rep}.

$$\overrightarrow{F_{res}} = \overrightarrow{F_{att}} + \overrightarrow{F_{rep}} \tag{11}$$

When an obstacle is inside the sensing envelope, the commanded yaw angle, ψ_{cmd}, is calculated as follows.

$$\psi_{cmd} = \cos^{-1}\left(\frac{F_{res}^2 + F_{att}^2 - F_{rep}^2}{2F_{res}\,F_{att}}\right) \tag{12}$$

In absence of obstacle in the sensing envelope, the commanded yaw angle is calculated as follows.

$$\psi_{cmd} = Err_{\psi} + 0.75Err_L - 90 \tag{13}$$

Where,

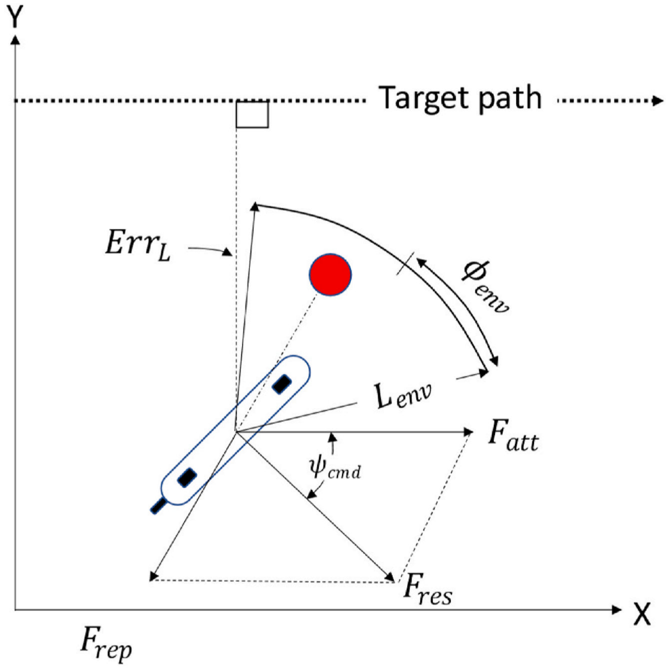

Fig. 5. Schematic diagram for collision avoidance under strategy 2. The mission of these experiments is that the vessel requires to maintain its position on the target path and avoid collision that comes along the way.

Err_ψ = yaw error, difference between the slope of the desired path and the vessels instantaneous yaw angle

Err_L = Longitudinal error, perpendicular distance between the vessel *C.O.G.* and desired path

2.2.3. Strategy 3

For strategy 3, a sensing envelope with a circular profile of radius, R_o, around the vessel is considered as shown in Fig. 6a. The robotic vessel feels a unit attraction force, $F_{att} = 1$, parallel to the target path. On the other hand, when any portion of the obstacle is inside this circular sensing area, it incurs a repulsive force, F_{rep}, from the *C.O.G.* of the robotic vessel perpendicularly away from the target path. Unlike the previous two strategies, F_{att} and F_{rep} are perpendicular to each other and directs the robotic vessel away from the obstacle to avoid collision.

The magnitude of the repulsive force is calculated as follows.

$$F_{rep} = K_{rep} e^{-\left(\frac{D_{obs}}{R_o}\right)} \tag{14}$$

When, $R_o = 3\ R_{obs} + L_{hull}$

D_{obs} is the minimum distance between the vessel C.O.G. and surface of the obstacle. For this strategy, K_{rep} is a function of the relative angle between the heading of the robotic vessel and the orientation of the obstacle with respect to the longitudinal axis of the vessel, γ in Fig. 6a. This repulsive force factors not only takes into consideration the distance between the obstacle and the vessel but also its direction. Thus, the repulsive force will be maximum if the vessel is heading straight to the obstacle ($\gamma = 0^\circ$) and minimum if it is straight behind the vessel ($\gamma = 180^\circ$).

K_{rep} is calculated as

$$K_{rep} = \cos\left(\frac{\gamma}{2}\right)\left|\cos\left(\frac{\gamma}{2}\right)\right| \tag{15}$$

Fig. 6b shows the magnitude of K_{rep} as a function of γ. K_{rep} reaches maximum value when $\gamma = 0$, meaning that the vessel is heading towards the center of the obstacle, and gradually decreases as γ increases, recaching a minimum value of zero at $\gamma = 180^\circ$. The later situation happens when the obstacle is right behind the vessel.

The magnitude F_{res} is calculated as follows.

$$F_{res} = \sqrt{F_{att}^2 + F_{rep}^2} \tag{16}$$

Then ψ_{cmd} can be calculated as follows.

$$\psi_{cmd} = \tan^{-1}\left(\frac{F_{rep}}{F_{att}}\right) \tag{17}$$

In absence of the obstacle inside the sensing circle, ψ_{cmd} is calculated as follows.

$$\psi_{cmd} = Err_\psi + 0.75 Err_L - \frac{\pi}{2} \tag{18}$$

3. Experimental setup

Fig. 2 shows the schematic diagram for the collision avoidance experiment conducted in this work. To avoid potential damage of the vessel, we considered a virtual obstacle that was fixed in time and space. The dimension and position of the static obstacle and target path is predefined. After processing the image, the position of the two markers on top of the vessel is resolved, based on which the position and yaw angle of the vessel is calculated. Using these values and chosen strategy, the commanded yaw angle (ψ_{cmd}), and subsequently, α_{cmd} is calculated, which is sent to the robotic vessel via a radio frequency (RF) signal. All the experiments were conducted at the surface of the water in the exterior pool at Florida Atlantic University SeaTech Campus.

Fig. 7 shows a snapshot taken by webcam at the start of an experimental case. The red circle and dashed line represent the obstacle and the target path respectively. Each experimental case starts with manually locating the markers from the first snapshot in the computer screen. The code is capable of continuously tracking the markers at each control loop. Table 1 shows the experimental parameters considered for all the strategies. Overall, the obstacle diameters considered are 0.27m, 0.54m and 0.81m. The sensing envelop angle considered in this work are 25°, 30° and 60°.

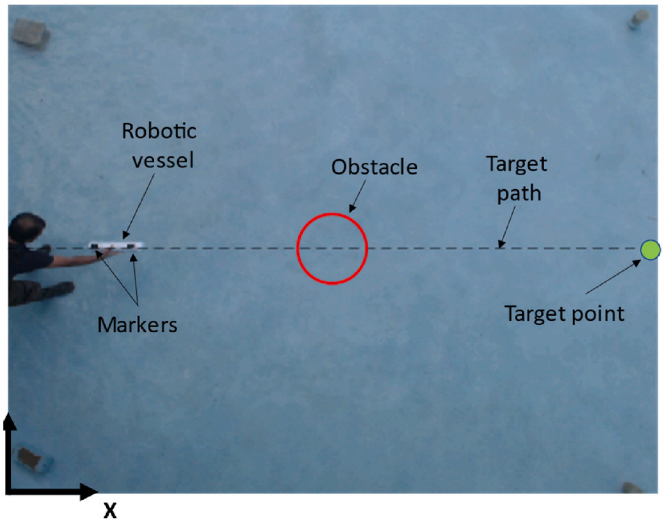

Fig. 7. Initial snapshot captured by the webcam during one experiment, illustrating key parameters associated with obstacle avoidance.

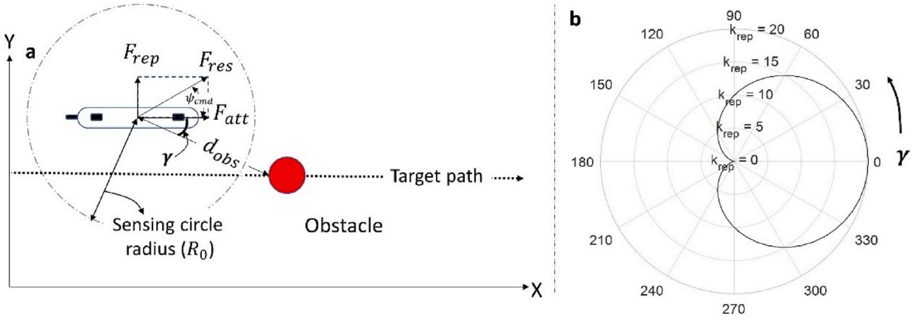

Fig. 6. Schematic diagram for collision avoidance strategy 3 a shows F_{rep} has a direction perpendicular to the desired path. Rather than having a sensing envelope, here we consider a sensing circle around the obstacle. The presence of the obstacle inside this circle will result in non-zero F_{rep}, which is proportional to the factor k_{rep}. Subfigure b plots k_{rep} as a function of difference between heading angle and direction from the vessel to the obstacle in polar plot.

Table 1
Parameters for strategy 1–3 experimental cases.

Strategy	Mission	Obstacle diameter (m)	Sensing envelope angle (φ_{env})
1	Target point	0.27, 0.54, 0.81	25, 30
2	Target path	0.54	30, 60
3	Target path	0.27, 0.54	-

4. Results and discussions

Fig. 8 shows robot path for an experimental case with no obstacle present in its path. The green line represents the target path, and the yellow-red path represents the measured position of the robotic vessel from initial (t_i) to final time (t_f) of reference. At time t_i, the robotic vessel starts traveling with a lateral offset from the mission path along Y-axis. As the robot gradually moves forward, it slowly corrects its heading and position, eventually merging to the target path.

The three lines in Fig. 9 represents experimental cases for three different strategies. These three cases consider one obstacle with equal diameter of 0.54m. The lines from darkest to lightest represent strategy 1 to 3 respectively. In addition to avoiding collision with obstacle in strategy 1, the mission is to reach the target point (green circle). On the other hand, the mission for strategy 2 and 3 is to merge with the target path (dashed line). Among the three cases, strategy 1 reaches destinations by traveling in a very close vicinity to the obstacle. For strategy 2, once the obstacle is avoided, the robotic vessel makes a sharp change to its path to go back to the mission path. Although strategy 3 takes the longest path to bounce back to its mission path, it has the smoothest transition from obstacle avoidance to come back to the mission path. Note that all experiments were conducted in a pool (water depth = 0.6 m) that was exposed to external weather. As a result, environmental parameters, such as wind speed and direction may vary as each experiment progresses.

Fig. 10 compares time series data of different parameters for the cases considered in Fig. 9. For each case considered, consistency in line characteristics is maintained in the plots shown in Figs. 9 and 10. In Fig. 10, subfigure *a* compares time data of distance between the robotic vessel and the obstacle, D_{obs}. During strategy 1, the robotic vessel passes very close to the obstacle surface while reaching the target point, as seen in Fig. 9. For strategy 2, as soon as the obstacle is away from the sensing envelope, the vessel came back to the mission path very quickly. Fig. 10 *b* and *c* show the time data of yaw angle, ψ, and desired yaw angle, ψ_{cmd}. In the event of the obstacle getting away from the sensing envelop, an abrupt change in ψ_{cmd} can happen. For example, sharp change in ψ_{cmd} is observed for strategy 1 and 2 at $T\sim11.5$sec and T~18sec respectively in

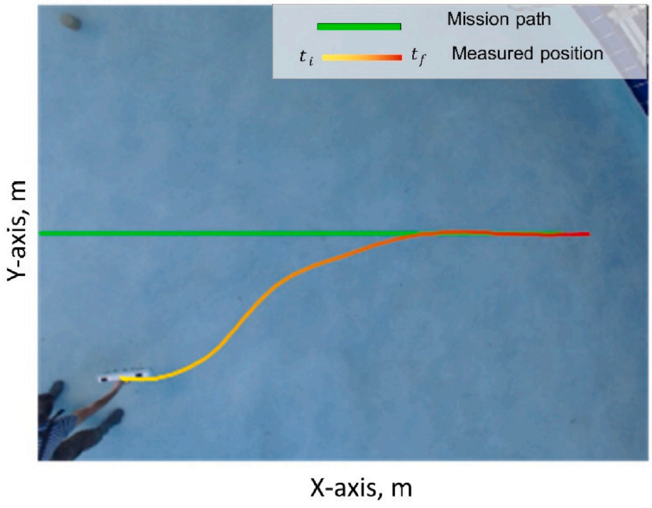

Fig. 8. Robot path with no obstacles present in its path.

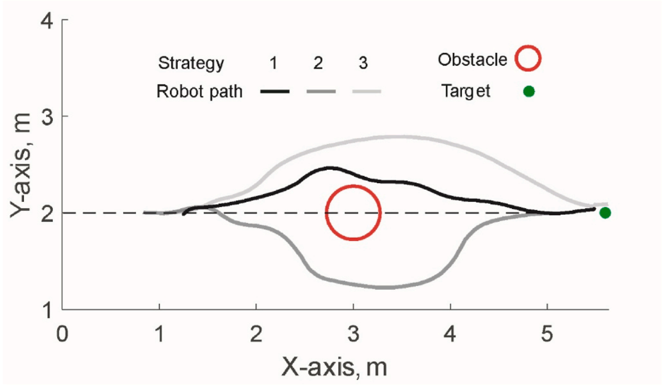

Fig. 9. Robot path comparison for three different strategies. All experiments consider the same obstacle diameter of 0.54m, located at the same longitudinal distance from the vessel's starting point. Here we considered experimental run 2 for strategy 1, experimental run 1 for strategy 2 and experimental run 1 for strategy 3. As mentioned earlier, strategy 1 considers a point target, whereas strategy 2 and 3 consider a mission path. Both experiment for strategy 1 and 2 considers envelope aperture (ψ_{env}) of 30° (total envelope angle of aperture 60°).

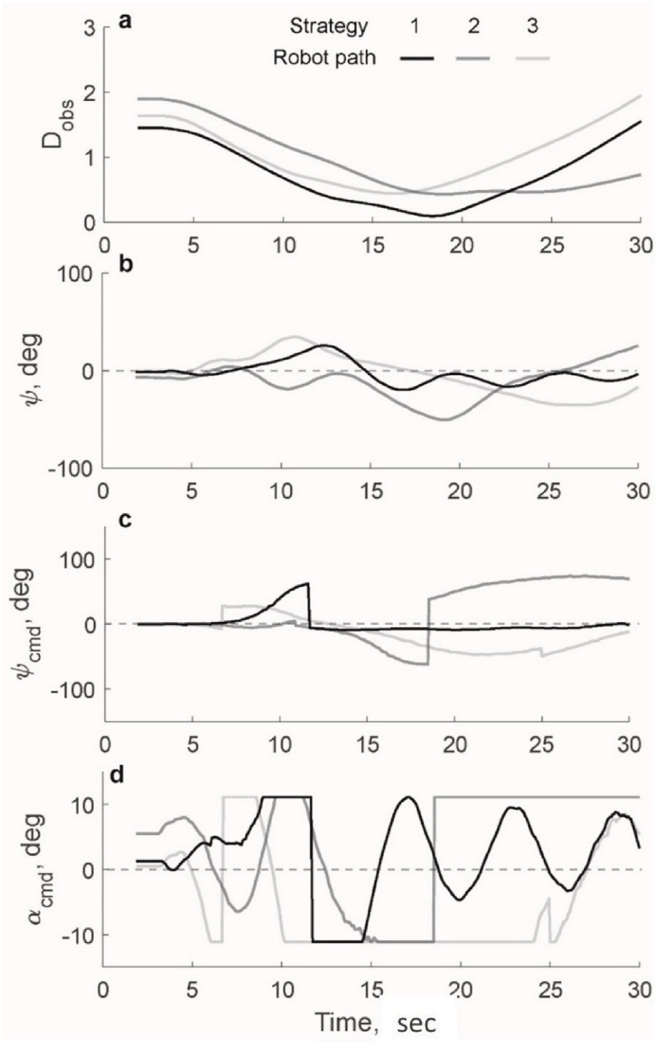

Fig. 10. Time series for different angular dataset for three different strategies. a shows time series of distance of the center of the robot from the obstacle surface. b, c and d plots time series of yaw angle, commanded yaw angle and commanded alpha angle in the fin.

Fig. 10c. To avoid this scenario, strategy 3 considers a “sensing circle” around it to detect the presence of the obstacle. The repulsive force is a function of γ, as shown in Fig. 6b. This results in a smoother transition of the vehicle back to its mission path, which is reflected in Figs. 9 and 10b-c.

Fig. 11 shows three key time steps for the cases considered in Figs. 9 and 10. This figure shows the vessel and the sensing envelope with respect to the obstacle at key time instants. In addition, the path of the vessel (solid black line) and target path (dashed black straight line) or target point (green circle) are shown. Fig. 11a–c, d-f and g-i represents cases for strategy 1, 2 and 3 respectively. We can observe that for strategy 1 at $T = 5$s, the obstacle is outside the sensing envelope, i.e., $F_{rep} = 0$. At this point, the robotic vessel swims towards the target point without any change in course. While this strategy is more efficient to get to the target point, the narrow envelop of the sensing volume can result in the vessel passing the obstacle too closely. Moreover, fluctuations on the yaw angle could result in situations where the obstacle might be in and out of the sensing envelop and be prone to discontinuities in the commanded yaw.

Fig. 12 a-c show time series of ψ_{cmd}, ψ_{err} and $\int \psi_{err}$ for three cases considered in Fig. 9. In Fig. 12a, for strategy 3, we see a sharp rise in ψ_{cmd} at ~7sec, when the obstacle enters the sensing circle for the first time. Unlike strategy 1 and 2, the reason behind the sudden change in ψ_{cmd} for strategy 3 is that F_{rep} always acts perpendicular to the target path. This results in a sharp increase in ψ_{cmd}. In addition, at the moment when obstacle enters the sensing circle, the equation for calculating ψ_{cmd} is changed from equation (18)–(17) due to non-zero value of F_{rep}. This results in even higher ψ_{err}.

In Fig. 11b, a strategy 1 case, the obstacle is seen inside the sensing envelope, which results in a non-zero F_{rep}. This results in a large yaw error (ψ_{err}) that causes a change in course of the vessel to avoid collision with the obstacle. The time instant at which the obstacle just moves out of the sensing envelope (T~13s), we see a sharp change in the ψ_{cmd}, as seen in Fig. 10c. At T = 15s, it is seen that the obstacle is outside the sensing envelope and vessel path becomes more aligned towards the target.

For strategy 2 at T = 10s as seen in Fig. 11d, the obstacle is outside the sensing envelope. After a while, in Fig. 11e, the obstacle is found inside the sensing envelope, which results in significant increase in ψ_{cmd} and ψ_{err} shown in Fig. 12a and b, causing the vessel to sway away from the obstacle to avoid collision. After few seconds in Fig. 11f, as the vessel moves forward, the obstacle gets out of the sensing envelope (T = 20s), meaning that F_{rep} became zero. This causes a sharp change in ψ_{cmd} in Fig. 12a, causing the vessel to rapidly change its direction to come back to the mission path.

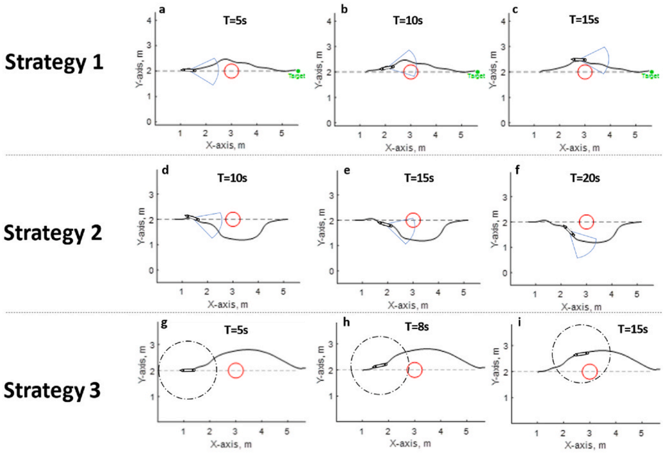

Fig. 11. Illustration of different time-steps for strategy 1, 2 and 3 plotted in previous figures. For each strategy, we have three figures showing three time-steps.

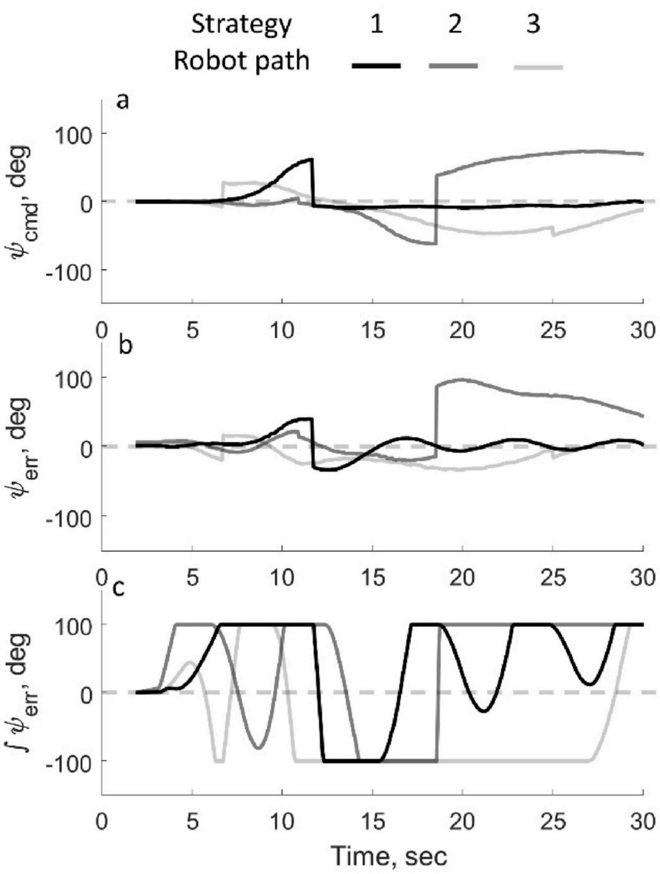

Fig. 12. Time series comparison for ψ_{cmd}, ψ_{err} and $\int \psi_{err}$ for three strategies.

Fig. 11g–i shows three time steps for strategy 3. At T = 5s, the vessel is yet to encounter the obstacle inside its sensing circle. At this time step, no action is taken to avoid collision, which is confirmed by ψ_{cmd} Fig. 12a, as it does not show any major change in its value at this time instant. At T = 8s shown in Fig. 11h, the obstacle in found inside the circular sensing envelop. This results in a change in ψ_{cmd}, and the vessel changes its course to avoid collision with the obstacle in its path. At T = 15s, the obstacle is still inside the sensing circle, but a larger magnitude of γ angle results in a lower magnitude of F_{rep} . This way the vessel avoids abrupt change in ψ_{cmd} and slowly converges to the mission path after avoiding collision with the obstacle.

Fig. 13 shows the time series data of yaw velocity the cases shown in Figs. 9–12. Here, the case considered under strategy 1 has the highest peak among all the cases considered in this figure. Similar peak values are also observed for strategy 2. On the contrary, strategy 3 has a smaller number of peaks and, between ~13 and 22 s, there is small variations in $\frac{d\psi}{dt}$. In this time interval, the vessel avoids collision with the obstacle and slowly merges with the target path. In general, large peaks in $\frac{d\psi}{dt}$ results from any abrupt changes in ψ_{cmd} and ψ_{err}. Strategy 1 and 2 requires the robotic vessel to travel less path to avoid the obstacle, but it comes with a penalty of abrupt change in yaw angle. When the sensing envelope is used to detect the obstacle as in strategy 1 and 2, the robotic vessel fails to sense an obstacle located very close to its body but oriented in such a way that the obstacle remains outside the sensing envelope. This is analogous to the scenario when a vehicle is located in the blind spot of another vehicle. For strategy 3, this problem is minimized, as the sensing circle around the robotic vessel helps to make smooth transition from avoiding the obstacle to merging to the target path. In Fig. 13, the standard deviation of $\frac{d\psi}{dt}$ for first 22sec for strategy 1, 2 and 3 are 6.1104 deg/s, 7.3051 deg/s, 5.1454 deg/s. And between 12 and 22sec, the

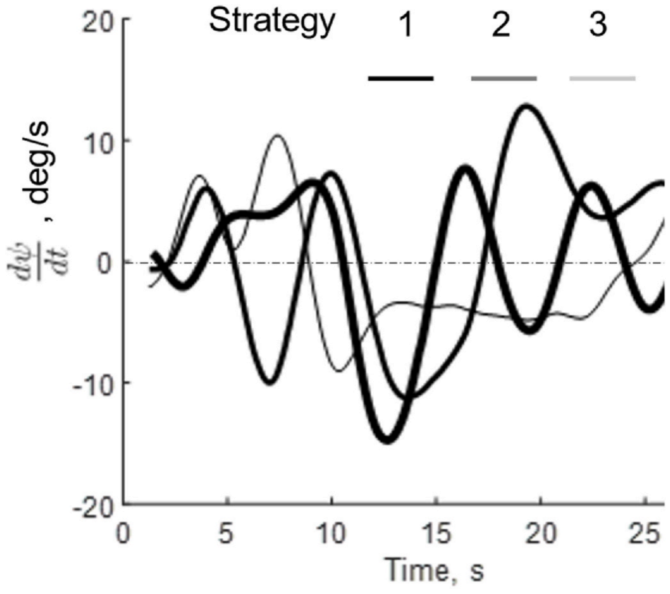

Fig. 13. Time series data for absolute yaw velocity for cases considered in Fig. 10 and 12. Yaw velocity for Strategy 3 remains steady between 13 and 22 s time intervals.

standard deviation becomes 7.1244 deg/s, 8.5610 deg/s and 1.4210 deg/s respectively. Between 12 and 22 s, for all strategies the robotic vessel finishes avoiding collision with the obstacle and starts merging with the target path. This indicates that the robotic vessel exhibits the lowest change in yaw velocity for strategy 3 compared to other strategies considered in the present work, which is reflected by the smoother transition of the robotic vessel with the mission path.

Fig. 14 plots three different experimental cases for strategy 1. For cases 1 to 3, the vessel path lines thicker to thinner, whereas, for obstacle, the red circle is darkest for the first case, and lightest for the third case. The obstacle diameter considered for the three cases were 0.27m, 0.54 and 0.81m respectively. Although during cases 1 and 2, the vessel was successful in avoiding the obstacle, the vessel collided with the obstacle during case 3. This result suggests that the strategy might be sensitive to the obstacle dimension and not best suited for large obstacles. However, the vessel successfully reached its destination in all cases.

Fig. 15 shows path of robotic vessel for two cases under strategy 2.

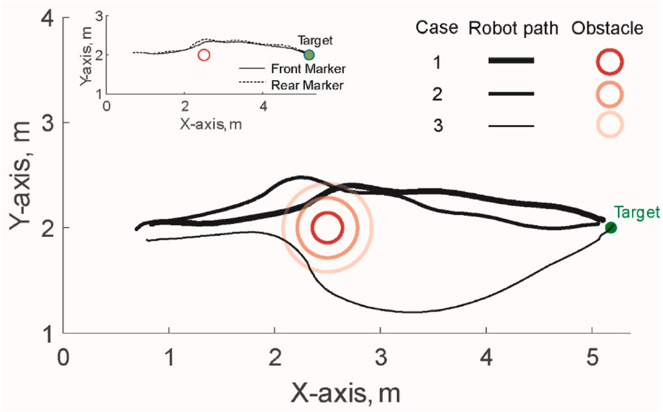

Fig. 14. Vessel path plotted for three different experiments under strategy 1. The objective of these experiments is to avoid the programmed obstacle and reach the destination point (labelled as target). Inset shows front and rear marker position for run 1. For run 1, 2 and 3, the diameters of the virtual obstacles are 0.27m, 0.54m and 0.81m, with envelope aperture of 25°, 30° and 30° respectively.

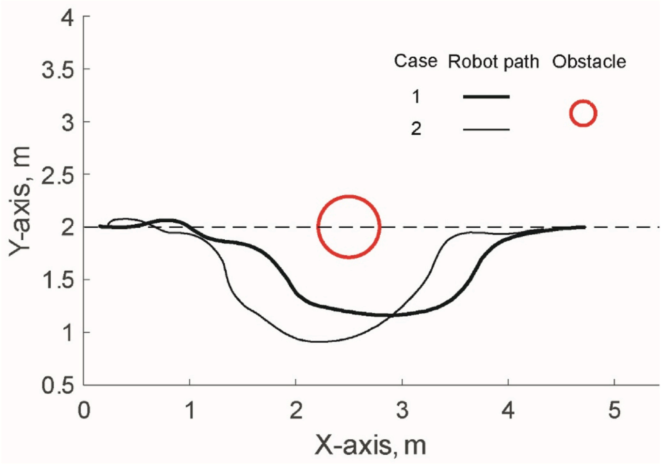

Fig. 15. Vessel path plot (solid lines) for two cases, under strategy 2. Both cases consider the same circular obstacle, with diameter 0.54m. Here, the mission objective is to keep on the target path (dashed line) while avoiding collision with an obstacle (red circle) encountered in the path. The only difference between these two experiments is the collision envelope aperture, which is 30° and 60° for cases 1 and 2 respectively.

The obstacle diameter considered for both cases was 0.54m. During both occasions, the vessel was successful in avoiding collision with the obstacle in both cases. Note that, for strategy 2, F_{att} is parallel to the mission path. When obstacle is not present inside the sensing envelope, the recipe for ψ_{cmd} in strategy 2 is different than strategy 1. In general, the time and path the vessel incurs to avoid an obstacle in strategy 2 is higher than it is in strategy 1.

Fig. 16 shows vehicle path for two different cases under strategy 3. The obstacle diameter considered for these three cases are 0.54m and 0.27m respectively. For both cases, the vessel avoided collision with the obstacle. For case 2, the initial transverse position of the vessel was away from the mission path. Initially, for this case, the vessel moves closer to the mission path, until the obstacle comes inside its sensing circle. Once the obstacle was inside the sensing circle, the vessel starts to sway away from the obstacle and mission path to avoid collision. One common observation for strategy 3 is that it does not result in sharp change in path after leaving the obstacle. The reason behind is that F_{rep} is a function of the orientation of the obstacle with respect to the heading angle of the vessel. The magnitude of F_{rep} decreases smoothly as γ increases,

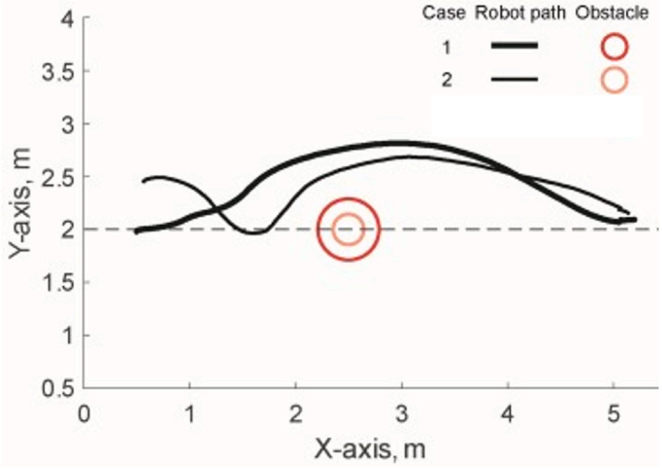

Fig. 16. Vessel path plotted for two different cases under strategy 3. The objective of this strategy is to avoid collision with obstacle and reach the target path. For cases 1 and 2, the diameters of the obstacles are 0.54m and 0.27m respectively.

resulting in a smoother transition of the vehicle to the mission path immediately after avoiding collision with the obstacle. Note that, for this case the obstacle does not suddenly disappear from the sensing envelope, but the repulsive force is weighted based on γ. This smooth transition is favorable for the integrity of the elongated fin propulsion unit consisting of thin rays, each directly coupled and actuated by an individual motor. Abrupt change in commanded yaw angle may damage the coupling between the motor and the ray, leading to malfunction of the fin.

5. Conclusions

Elongated ribbon fin propulsion can provide excellent maneuverability to navigate in complex underwater environments. However, the application of this propulsion method to effectively provide the motion control to the underwater vehicle to avoid collision requires the evaluation of collision avoidance methods in conjunction with this bio-inspired propulsion system and sensing capability. Toward that effort, we considered an underwater vehicle with a single undulating fin running along the length of the robot, which controls both forward motion and directional maneuvers. In this work, we experimentally evaluated different obstacle avoidance strategies with different sensing areas to evade a fixed obstacle along the path of the robotic vessel. Three collision avoidance strategies based on the potential field method were used to modulate the deflection of the rear portion of the traveling wave for directional control as the vehicle avoids a cylindrical obstacle and reaches a specific target point or path. Results from different cases are presented and discussed. All strategies considered were successful to avoid collision with the obstacle. For strategy 3, the vessel had a circular-weighted sensing around it, enabling the robotic vessel to avoid abrupt change in the commanded yaw angle that helped to smoothly transition to the mission path after avoiding obstacle collision. However, for this strategy the vessel tends to take a longer deviation path compared to the other strategies. Further, it is recommended that other obstacle avoidance strategies are studied for elongated fin propulsion to find the optimal condition.

CRediT authorship contribution statement

Mohammad Uddin: Methodology, Software, Data curation, Visualization, Writing – original draft, Writing – review & editing, Investigation. **Gonzalo Garcia:** Methodology, Software, Investigation. **Oscar Curet:** Conceptualization, Supervision, Funding acquisition, Project administration, Writing – original draft.

Declaration of competing interest

The authors declare that they have no known competing financial interests or personal relationships that could have appeared to influence the work reported in this paper.

Data availability

Data will be made available on request.

Acknowledgement

This material is based upon work supported by the National Science Foundation under Grant No. 1751548 to Dr. Oscar M. Curet.

References

Braginsky, B., Guterman, H., 2016. Obstacle avoidance approaches for autonomous underwater vehicle: simulation and experimental results. IEEE J. Ocean. Eng. 41 (4), 882–892.

Chakravarthy, A., Ghose, D., 2018. Collision cones for quadric surfaces in n-dimensions. IEEE Rob. Autom. Lett. 3 (1), 604–611.

Curet, O.M., Patankar, N.A., Lauder, G.V., MacIver, M.A., 2011a. Aquatic manoeuvering with counter-propagating waves: a novel locomotive strategy. J. R. Soc. Interface 8 (60), 1041–1050.

Curet, O.M., Patankar, N.A., Lauder, G.V., MacIver, M.A., 2011b. Mechanical properties of a bio-inspired robotic knifefish with an undulatory propulsor. Bioinspiration Biomimetics 6 (2), 026004.

Das, S.K., Dutta, A.K., Debnath, S.K., 2020. OperativeCriticalPointBug algorithm-local path planning of mobile robot avoiding obstacles. Indonesian Journal of Electrical Engineering and Computer Science 18 (3), 1646–1656.

Fan, X., Guo, Y., Liu, H., Wei, B., Lyu, W., 2020. Improved artificial potential field method applied for AUV path planning. Hindawi 2020.

Garcia, G., Uddin, M., Curet, O., 2020. Cambered undulating fin for heading control. In: APS Division of Fluid Dynamics Meeting Abstracts.

Garcia, G., Uddin, M., Verma, S., Curet, O., 2022. Reinforcement learning for maneuver control of a bio-inspired vessel with undulating fin propulsion. In: The 32nd International Ocean and Polar Engineering Conference, Shanghai.

Han, J., Seo, Y., 2017. Mobile robot path planning with surrounding point set and path improvement. Appl. Soft Comput. 57, 35–47.

Hawkins, O., Ortega-Jimenez, V., Sanford, C., 2022. Knifefish turning control and hydrodynamics during forward swimming. J. Exp. Biol. 225 (7).

I, K., Rivlin, E., 1998. Sensory-based motion planning with global proofs. IEEE Trans. Robot. Autom. 435–440.

Lapierre, L., Jouvencel, B., 2008. Robust nonlinear path-following control of an AUV. IEEE J. Ocean. Eng. 33 (2), 89–102.

Li, D., Wang, P., Du, L., 2019. Path Planning Technologies for Autonomous Underwater Vehicles-A Review. IEEE Access.

Liu, H., Curet, O.M., 2018. Swimming Performance of a Bio-Inspired Robotic Vessel with Undulating Fin Propulsion. Bioinspiration & Biomimetics.

Nelson, M., MacIver, M., 1999. Prey capture in the weakly electric fish Apteronotus albifrons: sensory acquisition strategies and electrosensory consequences. J. Exp. Biol. 202, 1195–1203.

Panda, M., Das, B., Subudhi, B., Pati, B.B., 2020. A comprehensive review of path planning algorithms for autonomous underwater vehicles. Int. J. Autom. Comput. 17 (3), 321–352.

Postlethwaite, C., Psemeneki, T., Selimkhanov, J., Silber, M., MacIver, M., 2009. Optimal movement in the prey strikes of weakly electric fish: a case study of the interplay of body plan and movement capability. J. Royal. Soc. Int. 6, 417–433.

J. Sosa and L. Adler, "Constrained Differential Evolution Optimization for Underwater Glider Path Planning in Sub-mesoscale Eddy Sampling".

Subramanian, S., Thomas, G., Asokan, T., 2012. Obstacle avoidance using multi-point potential field approach for an underactuated flat-fish type AUV in dynamic environment. Communications in Computer and Information Science.

Subramanian, S., George, T., Thondiyath, A., 2014. Rea-time obstacle avoidance for an underactuated flat-fish type autonomous underwater vehicle in 3d space. Int. J. Robot Autom. 29, 424–431.

Sunkara, V., Chakravarthy, A., Ghose, D., 2019. Collision avoidance of arbitrarily shaped deforming objects using collision cones. IEEE Rob. Autom. Lett. 4 (2).

Sunkara, V., Chakravarthy, A., Yi, X., Zuo, W., Chen, Z., 2020. Cooperative optimal collision avoidance laws for a hybrid-tailed robotic fish. IEEE Trans. Control Syst. Technol. 28 (4), 1569–1578.

Uddin, M.I., Curet, O.M., 2018. Modeling and control of a bio-inspired underwater vessel with undulating-fin propulsion. In: In OCEANS 2018 MTS/IEEE, 1–7. Charleston.

Uddin, M.I., Curet, O.M., 2019. Yaw Turning Experiments of a Bio-Inspired Vessel with Undulating Fin Propulsion. Bulletin of the American Physical Society, Seattle.

Uddin, M., Garcia, G., Curet, O.M., 2020. Scaling Law of Ribbon Fin Propulsion. Bulletin of the American Physical Society, Chicago.

Uddin, M., Garcia, G., Curet, O., 2022. Force scaling and efficiency of elongated median fin propulsion. Bioinspiration & Biomimentics 17 (4), 046004.